

Regular paper

3D-Printed frequency-scanned slot array in grating waveguide

Eduardo Garcia-Marin^{a,*}, Jose-Luis Masa-Campos^{a,*}, Pablo Sanchez-Olivares^b,
Beatriz Guilarte-Bellod^a

^a Department of Electronic and Communication Technology, Universidad Autónoma de Madrid, 28049 Madrid, Spain

^b Department of Signals, Systems and Radiocommunications, Universidad Politécnica de Madrid, 28040 Madrid, Spain

ARTICLE INFO

Keywords:

Linear antenna arrays
Slot antennas
Corrugated waveguides
Gratings
Layered manufacturing

ABSTRACT

In this work, a linearly-polarized frequency-scanned slot-antenna linear array fed by a travelling wave in grating waveguide is designed at 17 GHz. Additionally, the insertion of periodic gratings in the bottom broad-wall of the feeding waveguide reduces the guided wavelength of the fundamental propagating mode. Therefore, steering angles around broadside can be attained in the radiation pattern, contrary to conventional travelling-wave designs where grating lobes would inevitably appear. Furthermore, tuning posts are included in the radiating element design to mitigate the mismatch provoked by uniform phase feeding. A 16-element array is fabricated to validate the design, which experimentally shows a continuous angular scanning range of $\pm 10^\circ$ around broadside in the band from 16 to 18 GHz, with a peak gain of 18 dBi and a maximum gain drop of 4 dB.

1. Introduction

Frequency scanned array antennas provide the capability of reorienting the main radiation beam without electronic phase shifting circuitry [1]. Such feature is useful for radio-location applications such as marine or automotive radars [2,3], weather observations [4], or imaging systems [5]. Waveguide technology is well suited for these applications owing to its low dissipation and high-power handling capabilities. High gain waveguide antennas can be easily implemented in the form of slotted waveguide arrays. Traditionally, linear slotted waveguide arrays have been fed either by standing wave or by travelling wave. Resonant slotted arrays provide a fixed beam in broadside direction but with narrow-band response [6,7]. On the other hand, travelling-wave-fed slotted arrays provide not only larger operational bandwidths, but also frequency beam scanning due to the dependence between the slot spacing and the feeding phase [8,10]. However, the required array slot separation to achieve broadside radiation provokes strong grating lobe appearance. A reduction of the array slot distance to avoid this effect necessarily originates a high beam steering. This is unfeasible if the antenna must adapt to the supporting surface, as in airborne radars, where the antennas are installed on the nose of the aircraft for horizon line vision. This steering can be compensated by the insertion of metallic screws inside the waveguide [11]. Alternatively, a dielectric infill can be introduced to modify the propagation conditions in the waveguide, although losses will increase [12].

The grating waveguide (also known as corrugated waveguide) is a transmission line that includes, in at least one of its broadwalls, a corrugation created with periodic metallic gratings [13]. Similar gratings have been traditionally used in horn antennas to improve the radiation performance [14]. In a grating waveguide, the corrugation modifies the dispersion characteristics of the modes inside the guide. This is useful for instance to create electromagnetic stopbands as in soft and hard surfaces [15,16].

In this letter, a linearly-polarized frequency-scanning slot linear array antenna fed by a grating waveguide is designed and fabricated for Ku band operation. Travelling-wave feeding technique is implemented, contrary to the standing-wave topology in [16]. By properly designing the grating waveguide, a frequency-scanned beam around broadside direction will be obtained. In addition, the proposed grating provides further possibilities than conventional grating waveguide structures, since the grating is allowed to become narrower than the waveguide wall. The proposed antenna is a proof of concept at Ku band, though can be easily scaled to Ka or W bands, where linearly-polarized automotive radar systems typically operate [2,3,7].

2. Grating waveguide

The proposed slotted waveguide antenna is implemented in a grating waveguide (GW) with a rectangular cross-section of $13.5 \times 6.9 \text{ mm}^2$. The GW is defined as a rectangular waveguide where metallic gratings

* Corresponding authors.

E-mail addresses: eduardo.garciam@uam.es (E. Garcia-Marin), jose Luis.masa@uam.es (J.-L. Masa-Campos), pablo.sanchezo@upm.es (P. Sanchez-Olivares).

<https://doi.org/10.1016/j.aeue.2021.153866>

Received 1 September 2020; Accepted 16 June 2021

Available online 18 June 2021

1434-8411/© 2021 The Authors.

Published by Elsevier GmbH. This is an open access article under the CC BY-NC-ND license

(<http://creativecommons.org/licenses/by-nc-nd/4.0/>).

are periodically placed along the bottom broad-wall (Fig. 1(a)). These gratings effectively modify the propagation constant β of the fundamental propagating mode TE_{10} in the GW [16,17]. The objective is to increase β , thus reducing the guided wavelength λ_g of mode TE_{10} owing to the fact that $\lambda_g = 2\pi/\beta$. This way, broadside radiation without grating lobes will become feasible as long as $\lambda_g < \lambda_0$, with λ_0 the free-space wavelength.

In order to attain this objective, the behavior of a grating is investigated within a unit-cell of the GW. The unit-cell is formed by a short waveguide section of length d with a single grating (Fig. 1(b)). Cascading several of these unit-cells define a GW section. To obtain the propagation constant of mode TE_{10} (β) in the GW, an eigenmode calculation and Floquet analysis is performed in a unit cell [18]. In first place, a parametric sweep of the grating width and height (w and h in Fig. 1(b)) has been performed (the grating length l and the spacing d between gratings remain fixed). The β values obtained at 17 GHz in this study are plotted in Fig. 2(a). In addition, the guided wavelength (λ_g) and the impedance of mode TE_{10} (Z_{TE10}) associated to each value of β can be read in the same plot. As a reference, in a rectangular waveguide with the same cross-section as the GW but without grating, β is 269.5 rad/m at 17 GHz, λ_g is 23.30 mm, and Z_{TE10} is 498.1 Ω . Fig. 2(a) shows that as the grating height h raises, β rapidly increases as well, reaching values over 500 rad/m for h around 3 mm (0.43 times the waveguide height b). Inherently, the guided wavelength λ_g is greatly reduced, attaining half the value of λ_g in a rectangular waveguide. Note that the grating width w is allowed to be $w < a$, which increases the maximum attainable β to about 550 rad/m, while for a conventional grating ($w = a$), β is limited to about 400 rad/m for the same h .

Following, w and h have been fixed to 7 mm and 2.7 mm respectively, while the grating length l and spacing d between gratings have been swept, yielding Fig. 2(b). These parameters have much lower impact on β than w and h . Thinner gratings (that is, lower values of l) slightly help increase β , although values under 1 mm will be mechanically weak. In conclusion, the grating height h is the main parameter to modify the propagation characteristics inside the GW, while the grating width w can be used for finer modifications.

Once the dispersion characteristics of the unit-cell of the GW have been studied, the scattering parameters of the unit-cell have been computed for different values of h (Fig. 3(a)). Even for $h = 1$ mm the reflection is worse than -20 dB, owing to the mismatch between Z_{TE10} in the GW and in the waveguide port. The reflection will worsen in a GW with several gratings, as the reflections will accumulate. To mitigate this issue, the spacing between gratings in the GW will be fixed to $d = \lambda_g/4$ at the design frequency. This way, the reflections will cancel out following the small-signal analysis found in [19], Eq. 2. Consequently, the travelling wave in the GW will experience a phase shift $\alpha = 90^\circ$ between consecutive gratings at the design frequency. Since the phase shift can be calculated as $\alpha = \beta d$, the unit-cell must be designed seeking the value of β that generates a 90° phase shift in a physical propagation distance of d . This means that $\alpha = 90^\circ$ can be attained with unit-cells of different length d , by modifying the grating dimensions as to obtain the required

β . In this work, d has been fixed to 3.5 mm due to antenna design restrictions that will be addressed in Section III. The phase of the transmission parameter S_{21} is plotted in Fig. 3(b), proving that the introduction of the grating increases the phase shift α with respect to a rectangular waveguide ($h = 0$ mm). A grating height h between 2 and 3 mm is required to obtain $\alpha = 90^\circ$. The final dimensions of the unit-cell are $h = 2.73$ mm, $w = 7$ mm, $l = 1$ mm and $d = 3.5$ mm. For this unit-cell, the values at 17 GHz of β , λ_g and Z_{TE10} are 454.1 rad/m, 17 mm and 295.6 Ω , respectively. In Section III, this reflection-cancelling technique will be demonstrated with simulated results.

3. Radiating element in grating waveguide

After designing the GW, a transition is required to connect to a standard WR-51 waveguide and match their impedances. This transition is implemented as two $\lambda/4$ transformers defined by a GW section (Fig. 4(a)). The impedances of these transformers are obtained by the same procedure followed in Fig. 2. Following, radiation can be obtained from this matched GW by implementing a slot on the top broadwall, as in conventional travelling-wave slotted rectangular waveguides [9,10]. In order to obtain broadside radiation from a travelling-wave-fed slotted array, a spacing of λ_g between the slots is necessary to obtain the required uniform phase feeding. Since the gratings in the GW are spaced $d = \lambda_g/4$ to minimize reflections, the spacing between slots must be $4d = \lambda_g$. For this reason, the spacing d was set to 3.5 mm in Section II in order to satisfy the condition to avoid grating lobes ($\lambda_g < \lambda_0$). In summary, thanks to the insertion of gratings inside the waveguide, λ_g has been notably reduced to $\lambda_g = 0.85\lambda_0 = 15$ mm in the GW, and therefore grating lobes will be avoided. Note that, for this separation between radiating elements, a slotted array in rectangular waveguide would have a 39-degree main beam steering instead of broadside radiation as the proposed GW design.

Moreover, a slot acts as a discontinuity in the waveguide, provoking an undesired reflected wave in a similar way than the gratings of a GW. Large reflection will occur in a uniformly-fed array, as all the individual slot reflections will be added in phase at the input port [20], Eq. 2. Therefore, the only solution is to minimize the reflection produced by each single slot as much as possible. For this reason, the radiating element is designed as a 45-degree-inclined slot with a reflection-cancelling post, as proposed in [21]. However, in order to maintain the specified vertical polarization, such structure is mirrored, becoming a cross-slot with two reflection-cancelling posts as shown in the top view of Fig. 4(b). The fields radiated by each of the two slots in the cross have orthogonal polarizations and identical phase. In this manner, the total field radiated by the cross-slot is linearly polarized along y-axis. Besides, the cross-slot is narrower in the x-axis than a transverse slot, and thus its excitation will be less affected by the presence of the matching post.

The performance of this radiating element is assessed by simulation of the structure in Fig. 4(a). A GW with 9 gratings is terminated in both ends with WR-51 waveguides and the corresponding impedance

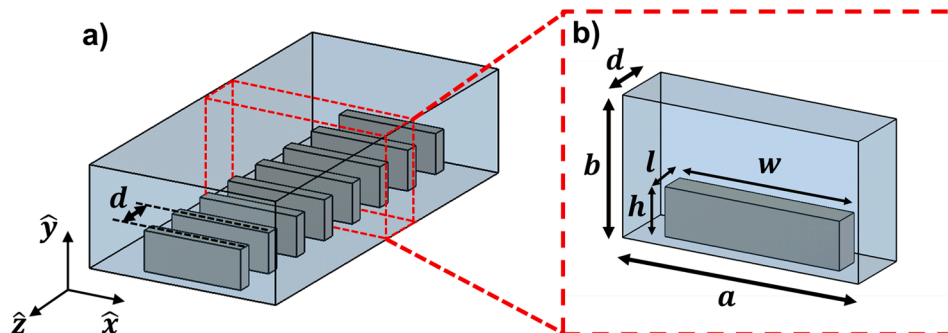


Fig. 1. a) Perspective view of a grating waveguide. b) Detail of a unit-cell of the grating waveguide.

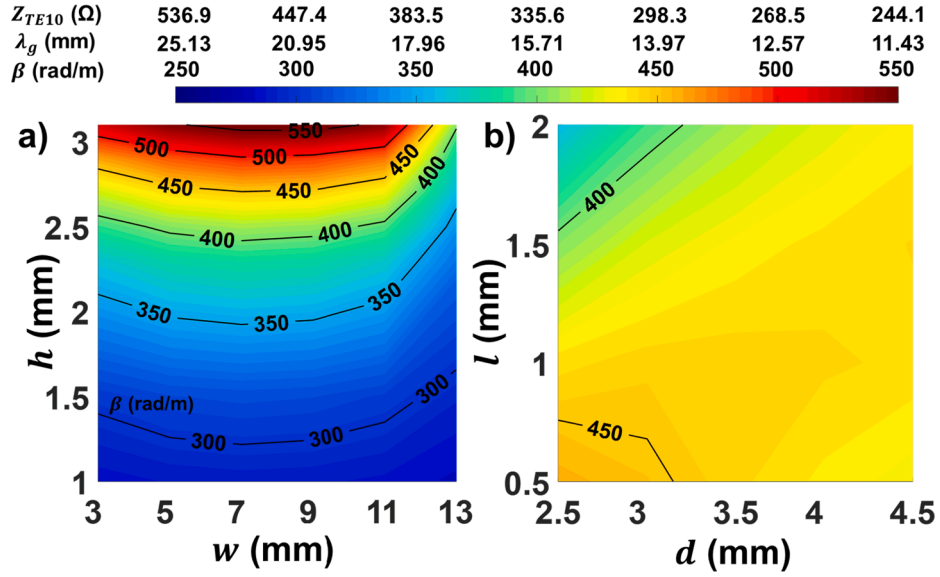


Fig. 2. Evaluation of β , λ_g and Z_{TE10} in the GW at 17 GHz for different values of a) w and h (for $l = 1$ mm and $d = 3.5$ mm), b) l and d (for $w = 7$ mm and $h = 2.73$ mm).

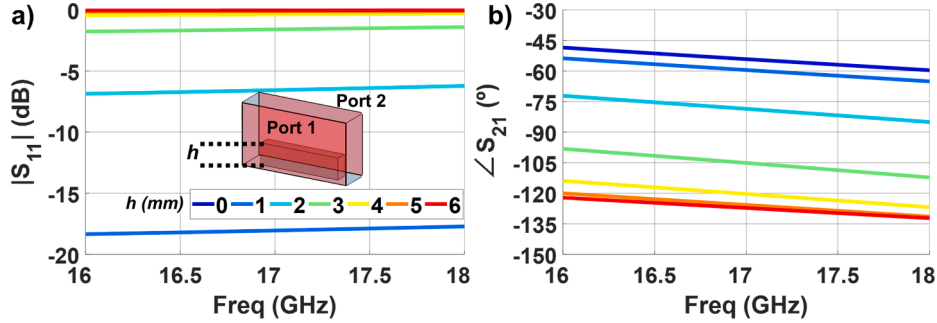


Fig. 3. S-parameter simulations of a unit-cell of the grating waveguide for different grating heights (h), and $w = 7$ mm, $l = 1$ mm and $d = 3.5$ mm. a) Matching coefficient. b) Phase of the transmission parameter.

transformers. The top broadwall of the GW is defined by the ground plane of a single-sided dielectric substrate (Taconic RF-35, $\epsilon_r = 3.5$) with 0.5-mm thickness. The cross-slot is etched in that ground plane, and the dielectric cover helps reduce the effective wavelength and thus the slot length [22]. The use of a dielectric substrate for the slot implementation enables rapid prototyping of different slot lengths within the university facilities, though for high power applications dielectric-free alternatives should be explored.

The proposed radiating element will be used in a travelling-wave array with uniform amplitude and phase distribution. In order to produce this illumination, each element will couple a certain amount of power from the travelling wave. Such amount is described with the coupling coefficient (C_{coup}) [Eq. 3], which is highly determined by the slot length [23]. Therefore, different lengths l_s of the cross-slot have been evaluated (Fig. 4(c)). At 17 GHz, the maximum C_{coup} is -4.5 dB, obtained with a cross-slot resonant length of 6.1 mm ($0.35\lambda_0$). This length is far from the conventional slot resonant value of $0.5\lambda_0$ due to the dielectric cover of the slot. Besides, each C_{coup} is achieved with an optimal performance in terms of S_{11} , which is attained by tuning both the position (y_p) and dimensions (l_p , w_p , h_p) of the reflection-cancelling posts. Minimum S_{11} is imposed around the center frequency, where the reflections of all the slots in the array will be added in phase. The S_{11} parameter for the different slot lengths is plotted in Fig. 4(d). As a baseline, the S_{11} curve of a GW with impedance transformers but without slot or matching posts is also represented. At 17 GHz, reflection under -40 dB is obtained except for the resonant slot ($l_s = 6.1$ mm).

Matching deteriorates as C_{coup} increases, as the slot becomes a more abrupt discontinuity in the GW. In any case, the matching performance is better than -13 dB in the whole band.

Furthermore, the electric field has been simulated at 17 GHz in the structure in Fig. 4(a), for the optimal slot design when $l_s = 6.4$ mm. The amplitude of the z-polarized component is shown in Fig. 4(e), from a top-view perspective, on the xy cut-plane of the GW top broadwall. The distance between amplitude maxima gives the guided wavelength in each waveguide section. It is evident that the GW greatly reduces the guided wavelength, as the maxima are closer than in the WR-51 sections. Furthermore, the coupling from the slot is observable as well, since the maxima show lower amplitude after the cross-slot (propagation is towards $+y$). Besides, Fig. 4(f) shows the total electric field in a yz cut-plane longitudinal to the propagation direction, and in the middle of the GW width. In this plot, the z-polarized pure TE_{10} mode can be clearly seen in the WR-51 rectangular waveguide sections. However, this mode is altered in the GW, where a y-polarized field component appears due to the presence of the periodic gratings. In addition, Fig. 4(g) shows the total field in a xz cut-plane, transverse to the propagation direction and placed just in the middle of the cross-slot. The field configuration is eminently z-polarized as in the TE_{10} mode present in the WR-51 sections. However, a x-polarized field component is present as well in the lower half of the side walls. In fact, the field configuration resembles that of a TEM-like mode in a ridge waveguide. The difference is the presence of a y-polarized field component as seen in Fig. 4(f): while in a ridge waveguide the ridge is continuous along the propagation direction, the

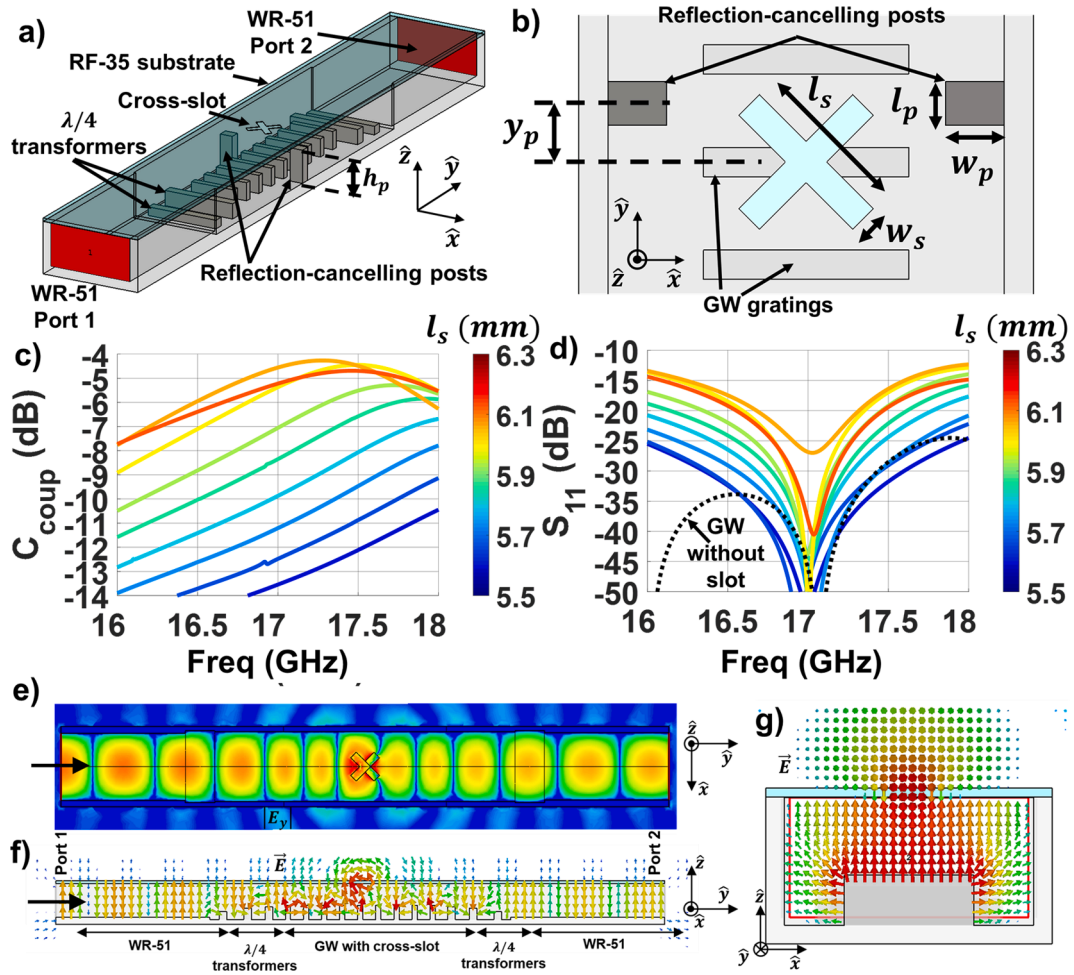


Fig. 4. Single radiating element in GW consisting in a cross-slot with two reflection-cancelling posts: a) bird view, b) top view, c) C_{coup} for different slot lengths, d) S_{11} for different slot lengths, e) amplitude (17 GHz) of the z-component of the electric field in a xy cut-plane at the top broadwall of the waveguide, when exciting port 1 for $l_s = 6.4\text{mm}$, f) electric field at 17 GHz (side view) in a yz cut-plane centered in the middle of the waveguide, when exciting port 1. g) Same field in a xz cut-plane centered in the cross-slot.

gratings in the GW are periodic, causing the appearance of the propagation-polarized field component. However, in the transverse plane (xz), the gratings act just as the ridge in the ridge waveguide: they effectively increase the waveguide width. The field amplitude variation

goes along a longer path due to the presence of the grating, thus decreasing the cutoff frequency and consequently, reducing the guided wavelength, as demonstrated already in Fig. 2.

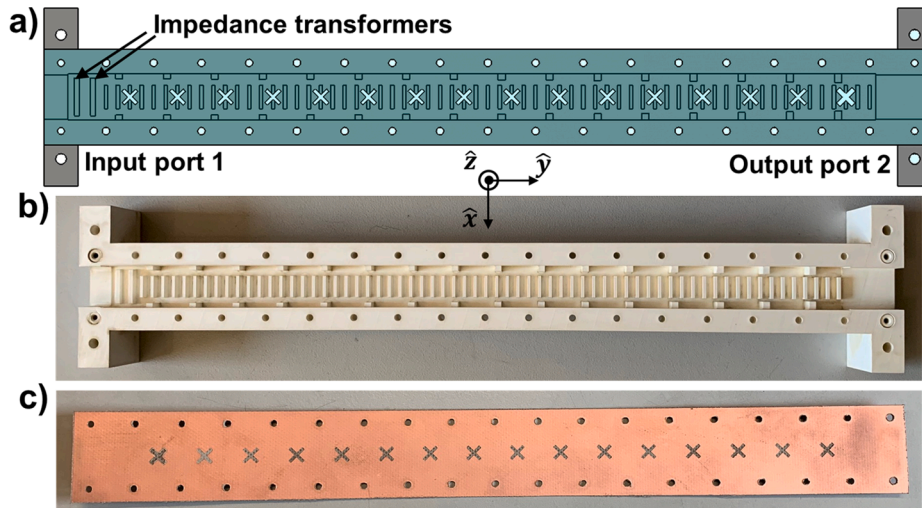


Fig. 5. 16-element cross-slot array antenna in GW: a) full-wave simulated structure, b) 3D-printed and silver-plated feeding GW, c) PCB-milled slot array.

4. Prototyping and experimental validation

Once the radiating element is characterized, the antenna array can be assembled. A 16-element array antenna with travelling-wave feed in GW is proposed (Fig. 5(a)), using the radiating element of Section III. In the detail of Fig. 5(a), the impedance transformers placed after the WR-51 input waveguide are indicated. The transformers at the output port 2 have been removed to miniaturize the antenna. The matching performance is not affected by this modification, since the travelling wave carries very low power after traversing the whole array and thus the reflection will be weak.

The array is designed as in conventional travelling-wave slotted arrays. The required C_{coup} for each element is derived with the formulation in [20], in order to achieve a uniform feeding distribution and a 17% non-radiated power lost in the output port 2 (−7.7 dB). For the proposed array, C_{coup} between −12.5 dB and −4.5 dB are needed, corresponding to slot lengths between 5.6 mm ($0.32\lambda_0$) and 6.1 mm ($0.35\lambda_0$).

The 16-element array antenna has been fabricated for experimental validation of the design. The feed line in GW technology has been manufactured by stereolithography combined with spray-based silver metallization (Fig. 5(b)). This structure is specially well suited for 3D printing, due to the presence of the gratings and reflection-cancelling posts. The cross-slot array is etched on the copper plane of a single-sided 0.5-mm-thick Taconic RF-35 substrate by PCB milling (Fig. 5(c)). In the final antenna assembly, the substrate is attached to the GW line by means of screws.

In first place, the scattering parameters have been measured (Fig. 6). The input matching coefficient S_{11} presents a worst-case value around −10 dB at 17.05 GHz. Slight discrepancies with simulations are caused by manufacturing tolerances. The transmission parameter S_{21} informs that the fabricated prototype is wasting less power than anticipated (−8.5 dB, or 14.1%, versus the simulated value of −7.7 dB, or 17%). The main cause are dissipation losses being higher than expected, as the dielectric substrate is characterized only up to 10 GHz. Slight leakage in the flanges and the seam between the array and the GW might contribute as well to power loss.

Following, the radiation patterns have been measured in the beam-scanning plane (yz-plane in Fig. 5). The results are shown in Fig. 7(a) normalized to the maximum achieved gain in the frequency band. Grating lobe appearance is noticeable for frequencies over 17.8 GHz due to larger phase shifts and electrical spacing between radiating elements, although staying in a relative level under −9 dB. As the detail of Fig. 7(b) demonstrates, a beam scanning of 20° is accomplished (from $\theta = -10^\circ$ to $\theta = +10^\circ$), which translates into a scan of 1 degree per 100 MHz. Relative cross-polarization levels, depicted in grayscale colors in Fig. 7(a), are under −25 dB, thanks to the high physical symmetry of the structure. Furthermore, a maximum gain drop of 4 dB is observed, which occurs for the highest frequencies due to the incipient grating lobe.

This is supported by the directivity and gain curves of Fig. 8. In order to interpret the results, it should be reminded that the maximum achievable directivity $D_{0,\text{max}}$ of an antenna with a physical aperture area A_{phys} can be estimated as

$$D_{0,\text{max}} = 4\pi \frac{A_{\text{phys}}}{\lambda_0^2}$$

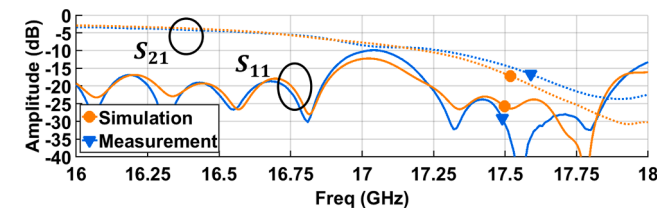


Fig. 6. Scattering parameters of the 16-element array antenna.

Where λ_0 is the free-space wavelength. However, in practice the antennas are incapable of attaining this value, due to an imperfect use of their physical aperture. Thus, in general, the estimated directivity of an antenna will be

$$D_0 = 4\pi \frac{A_e}{\lambda_0^2}$$

Where A_e is the effective aperture area of the antenna, which will be $A_e \leq A_{\text{phys}}$. This way, it is possible to define the aperture efficiency η_{aper} as

$$\eta_{\text{aper}} = \frac{A_e}{A_{\text{phys}}} = \frac{D_0}{D_{0,\text{max}}}$$

The ideal case where $\eta_{\text{aper}} = 100\%$ would be for an antenna capable of generating a uniform field on its aperture, both in terms of amplitude and phase. Nevertheless, realistic cases are those where the field at the aperture shows some amplitude and phase variation, thus reducing the aperture efficiency. In fact, it is possible to express such efficiency as the product $\eta_{\text{aper}} = \eta_{\text{amp}}\eta_{\text{ph}}$ where η_{amp} and η_{ph} measure how uniform the amplitude and the phase of the electric field are at the aperture, respectively.

In order to evaluate η_{aper} in this work, the value D_0 is obtained by full-wave simulations. As for $D_{0,\text{max}}$, the physical aperture area A_{phys} is calculated as a rectangle sized $12 \times 220 \text{ mm}^2$, which encloses the majority of the simulated radiated field by the array. Fig. 8 shows the aperture efficiency and the simulated directivity. The directivity shows an ascending behavior, which is expected as the electrical size A_e/λ_0^2 of the aperture increases. This is true up to 17.7 GHz, where grating lobes start to appear in the patterns of Fig. 7, thus degrading the directivity and dropping the aperture efficiency to 30% at 18 GHz. The peak aperture efficiency is 95% at 17 GHz. This is where the array feeding distribution has been designed to be uniform in amplitude and phase, thus maximizing the product $\eta_{\text{aper}} = \eta_{\text{amp}}\eta_{\text{ph}}$. Outside this frequency, the amplitude uniformity is degraded since the coupling coefficients of the slots differ from the design value at 17 GHz. Furthermore, the phase uniformity worsens as well, since a progressive phase shift is produced between radiating elements, due to the travelling-wave feeding topology.

Following, the radiation efficiency has been computed as

$$\eta_{\text{rad}} = \frac{G_{0,\text{sim}}}{D_{0,\text{sim}}(1 - |S_{11}|^2 - |S_{21}|^2)}$$

Where $G_{0,\text{sim}}$ is the simulated realized gain (which includes losses due to mismatch, wasted power at output port 2, and dissipation), and $D_{0,\text{sim}}$ is the simulated directivity. The factor $(1 - |S_{11}|^2 - |S_{21}|^2)$ eliminates the effects of mismatch and wasted power losses, which are present on the calculation of $G_{0,\text{sim}}$. Therefore, η_{rad} provides a measure of the antenna efficiency just in terms of dissipation losses. Simulations suggest that the radiation efficiency should stay over 90%. Since the waveguide is silver coated, dissipation losses mainly come from the dielectric substrate hosting the slots.

Finally, the total efficiency η_{total} has been estimated as

$$\eta_{\text{total}} = \frac{G_{0,\text{sim}}}{D_{0,\text{sim}}}$$

Contrary to the radiation efficiency, the total efficiency includes, aside from dissipation losses, the gain reduction due to impedance mismatch as well as power waste at output port. These losses cause the difference between the radiation efficiency and total efficiency curves in Fig. 8. The total efficiency varies through the frequency band according to the power waste at output port 2. At 17 GHz, the total efficiency is around 80%. Around 5% of efficiency drop is caused by dissipation loss (since the radiation efficiency is 95%), while the remaining 15% is

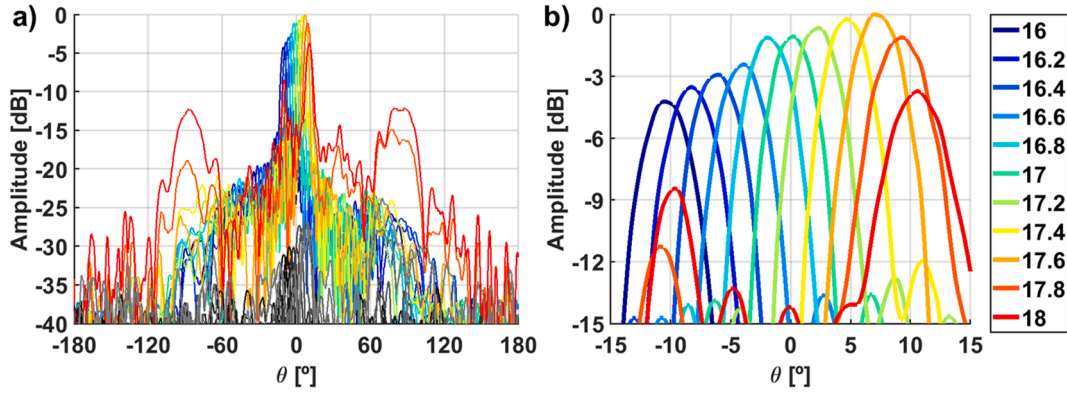


Fig. 7. a) Measured radiation patterns of the 16-element array antenna. Cross-polarization measurements are plotted in grayscale colors. b) Detail of the plot in a).

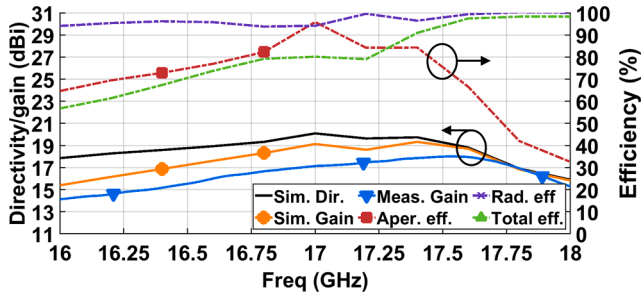


Fig. 8. Directivity, gain and simulated efficiency curves of the 16-element array antenna.

caused by mismatch and power waste. The efficiency increases at the upper frequency band since the power waste at output port 2 greatly diminishes.

The simulated realized gain shows the same behavior as the directivity, with a deeper decrease in the lowest frequencies as a result of higher power waste at output port 2 (see Fig. 6). However, the measured realized gain is around 1 dB lower than the simulated curve at 17 GHz. Slight additional losses may arise from the uncertainty in the dielectric substrate characterization, since the dissipation tangent at 17 GHz was extrapolated from the manufacturer data at 10 GHz. However, the main cause of the measured gain drop is actually a directivity decrease due to the split-block realization of the antenna prototype. The 3D-printed GW is slightly warped due to temperature and mechanical stress produced during the manufacturing. The warping provokes an imperfect electrical contact between the GW and the radiating array, and therefore power leakage is produced through that gap. This could be mitigated by using stopband metasurfaces [24], or by 3D-printing a single block antenna with the slots embedded in the GW body. In any case, the leaked signal is finally radiated, thus altering the radiation pattern. This is not noticed in

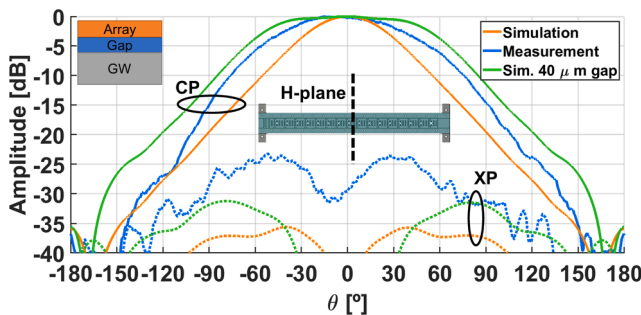


Fig. 9. H-plane radiation pattern at 17 GHz. The beamwidth is greatly increased due to leakage in the gap between the GW and the array.

the E-plane scanning patterns of Fig. 7, but in the H-plane, which is aligned with the gap that produces the radiation of the leaked power. Fig. 9 shows the simulated and measured H-plane radiation patterns at 17 GHz. In addition, a simulation including a gap with 40-μm thickness between the GW and the array has been carried out, proving that the H-plane beamwidth increases due to the gap. The 3-dB beamwidth in H-plane has increased from 54 to 83° owing to power leakage. This has a direct effect on the directivity, which can be estimated by the following formula [[25], Eq. 2-27]:

$$D_0 \approx \frac{41253}{\Delta\theta_{-3dB,E} \Delta\theta_{-3dB,H}}$$

Where $\Delta\theta_{-3dB,E}$ and $\Delta\theta_{-3dB,H}$ are the 3-dB beamwidths (in degrees) at E and H planes, respectively. Knowing that $\Delta\theta_{-3dB,E} = 4^\circ$ both in simulation and measurement, the simulated and measured directivities can be estimated with the beamwidths. A 1.4 dB directivity drop is produced by increasing $\Delta\theta_{-3dB,H}$ from 54 to 83°. For this reason, the measured directivity of the prototype, which unfortunately is not available, must have decreased due to power leakage, which explains the gain drop observed in the measurements. At higher frequencies, the measured gain converges with the simulation, since the grating lobe becomes the main cause of directivity degradation, masking the effect of power leakage on the radiation pattern.

Finally, Table 1 includes a comparison of different performance parameters with similar published works, in order to put results into context. Reference [21] proposes a K-Ka band planar array in post-wall or substrate integrated waveguide (SIW). Although travelling-wave feeding is used, there is no beam steering capability owing to the antenna topology. Besides, very large dissipation losses have been reported in the dielectric substrate, and hence low efficiency is obtained. Reference [11], published by some of the authors, consists in a travelling-wave slotted waveguide with three tuning screws in each radiating element. These allow to modify the phase excitation as well as to improve the impedance matching. This way, broadside radiation with no grating lobes becomes feasible, and very high efficiency is affordable, although the impedance bandwidth becomes somewhat limited. Reference [9] is a slotted waveguide design as well, and therefore the efficiency is high, although the scan angle is limited to 10°. In reference [26], a SIW leaky-wave solution is proposed, yielding a wide scan angle of 70° with low scan loss. However, the efficiency is limited to 60% due to the dielectric dissipation, and the aperture efficiency is around 40%. In order to improve the 10-dBi measured gain, a larger number of array elements should be used. However, this would increase propagation losses, and therefore the total efficiency reaches a limit with this kind of design. In reference [16], a GW array is presented, achieving high efficiency in a compact size. Nevertheless, standing-wave excitation is used, and thus no beam scanning is possible. Finally, the present work proposes a GW with travelling-wave feeding, which allows a 20° scan angle

Table 1

Comparison of the proposed antenna with similar published designs. The values are provided at the center frequency.

	Center freq f_0 (GHz)	Technology	Number of elements	Aperture size ($\lambda_0 \times \lambda_0$)	Gain (dBi)	Aperture eff. (%)	Total eff. (%)	Scanning	Scan loss (dB)	Scan with frequency (MHz/°)
[21]	25.8	PCB	84	5.2×11.2	22	98	22	No $\theta = 0^\circ$	–	–
[11]	11.5	Waveguide	5	0.8×3.2	14.5	97	90	17° $\theta = 4$ to 21°	5	*
[9]	10	Waveguide	9	0.7×6	13.7	44.4	79	10° $\theta = -5$ to $+$ 5°	1	100
[26]	10	PCB	20	0.4×4.9	10	40.6	60	70° $\theta = -23$ to $+$ 47°	1.2	34
[16]	12.5	Waveguide	8	0.8×4.3	15.8	88	89	No $\theta = 0^\circ$	–	–
This work	17	Waveguide	16	0.7×12.5	17.2	95	55	20° $\theta = -10$ to $+$ 10°	4	100

* Beam is mechanically steered in the same frequency.

across a 2-GHz bandwidth. Although the aperture efficiency is high, the total efficiency is low for a waveguide design, although the correction of the assembly issues should mitigate this problem. Besides, a larger number of array elements should allow a lower power waste at the output port, thus boosting efficiency. Finally, the use of a metallic feeding GW enables further capabilities than PCB-based designs: the design could be easily used in higher frequencies, in high power systems like radars or satellite communications, or in higher-directivity arrays with more elements.

5. Conclusions

A 16-element frequency-scanned travelling-wave slot array antenna has been designed and fabricated in Ku-band (16–18 GHz). The proposed antenna serves as a proof of concept of the use of grating waveguide technology in frequency-scanned arrays, which could be easily scaled for millimeter-wave satellite communications or automotive radar applications. The implementation of grating waveguide technology in the feeding line allows to achieve broadside radiation without grating lobe appearance by increasing the propagation constant in the guide. Compared with conventional grating waveguide designs, the corrugations presented in this work are narrower than the waveguide width, and therefore larger values for the propagation constant are attainable. Besides, in order to mitigate high reflection caused by in-phase feeding of the radiating elements, reflection-cancelling posts are placed near the slots. Experimental results yield a reflection coefficient better than -10 dB in the whole band, with a 14.1% non-radiated power at the design frequency. A 20-degree beam scanning range is accomplished, with a grating lobe level of -9 dB in the worst case. Noticeable gain drop is experimentally observed, which could be addressed with a single-block prototype fabrication.

Funding

This work was supported by the Spanish Government under grant TEC2016-76070-C3-1-R (Agencia Estatal de Investigación, Fondo Europeo de Desarrollo Regional: AEI/FEDER, UE).

Declaration of Competing Interest

The authors declare that they have no known competing financial interests or personal relationships that could have appeared to influence the work reported in this paper.

References

- [1] Ishimaru A, Hang-Sheng Tuan, Frequency scanning antennas, 1958 IRE International Convention Record, New York, NY, USA, 1961, pp. 101-109.
- [2] Tian C, Tian Y, Ma H, Wang C, Wang J. Small target detection for solid-state marine radar. In: 2016 CIE International Conference on Radar (RADAR), Guangzhou, 2016, pp. 1-4.
- [3] Khadom Mohsen Mowafak, Bin Mohamad Isa Mohd saari, Bin Awang Md Isa Azmi, Kaml Abdulhameed Muhannad, Lafta Attiah Mothana, Alsharaa Baseem. Novel and active technique for controlling the radiation pattern of the half-width microstrip leaky wave antenna array. AEU - Int J Electron Commun 2019;110.
- [4] Karimkashi S, Zhang G, Kishk AA. A dually polarized frequency scanning microstrip array antenna for weather radar applications. In: 2013 7th European Conference on Antennas and Propagation (EuCAP), Gothenburg, 2013, pp. 1795-98.
- [5] Fartookzadeh Mahdi, Armaki Seyyed Hossein Mohseni. Efficiency improvement and cross-polarization reduction of single-fed frequency-scan leaky wave microstrip antennas by using an M-shape metasurface as the WAIM layer. AEU - Int J Electron Commun 2020;116.
- [6] Ghorbani Saeid, Razavi Seyed Ali, Ostovarzadeh Mohammad Hossein, Farahbakhsh Ali. Development of a center fed slot array antenna with very low side lobes using ridge gap waveguide (RGW) technology. AEU - Int J Electron Commun 2020;125.
- [7] Pyne B, Akbar PR, Ravindra V, Saito H, Hirokawa J, Fukami T. Slot-Array Antenna Feeder Network for Space-Borne X-Band Synthetic Aperture Radar. IEEE Trans Antennas Propag July 2018;66(7):3463–74.
- [8] Schneider DA, Rösch M, Tessmann A, Zwick T. A Low-Loss W-Band Frequency-Scanning Antenna for Wideband Multichannel Radar Applications. IEEE Antennas Wirel Propag Lett April 2019;18(4):806–10.
- [9] Dolati Meisam, Saeed Majedi Mohammad. A wideband 45° inclined linear polarization travelling-wave slot array antenna with broadside radiation pattern. AEU - Int J Electron Commun 2019;106.
- [10] Sanchez-Olivares Pablo, Masa-Campos Jose-Luis, Garcia-Marin Eduardo, Barrio-Tejedor Diego, Kumar Pradeep. Dual-linearly polarized travelling-wave array antenna based on triple plus slots fed by square waveguide. AEU - Int J Electron Commun 2020;119.
- [11] Sanchez-Olivares P, Masa-Campos JL, Hernandez-Ortega J. Mechanical Technique to Customize a Waveguide-Slot Radiating Performance. IEEE Trans Antennas Propag Jan. 2018;66(1):426–31.
- [12] Host NK, Chen C, Volakis JL, Miranda FA. Ku-Band Traveling Wave Slot Array Scanned Via Positioning a Dielectric Plunger. IEEE Trans Antennas Propag Dec. 2015;63(12):5475–83.
- [13] Elliott R. On the theory of corrugated plane surfaces. Trans IRE Professional Group on Antennas Propag April 1954;2(2):71–81.
- [14] Baldwin R, McInnes PA. Corrugated rectangular horns for use as microwave feeds. Proc Instit Electrical Eng 1975;122(5):465–9.
- [15] Kildal P. Definition of artificially soft and hard surfaces for electromagnetic waves. Electron Lett 1988;24(3):168–70.
- [16] Yuan W, Liang X, Zhang L, Geng J, Zhu W, Jin R. Rectangular Grating Waveguide Slot Array Antenna for SATCOM Applications. IEEE Trans Antennas Propag June 2019;67(6):3869–80.
- [17] Balanis C. Advanced Engineering Electromagnetics. 2nd Edition. Wiley; 2012.
- [18] Mealy TK, Eshrah IA, Abulfadl TM. Solution of periodically loaded waveguides using the eigenmode projection technique. In: 2016 IEEE MTT-S International Microwave Symposium (IMS), San Francisco, CA, 2016, pp. 1-4.
- [19] Masa-Campos JL, Sierra-Perez M. Linearly Polarized Radial Line Patch Antenna With Internal Rectangular Coupling Patches. IEEE Trans Antennas Propag Aug. 2011;59(8):3049–52.

- [20] Masa-Campos JL, Klinger S, Sierra-Perez M. Parallel Plate Patch Antenna With Internal Rectangular Coupling Patches and $TE_{\rm N0}$ Mode Excitation. *IEEE Trans Antennas Propag* July 2009;57(7):2185–9.
- [21] Sehyun Park Y, Okajima J, Hirokawa, Ando M. A slotted post-wall waveguide array with interdigital structure for 45/spl deg/ linear and dual polarization. *IEEE Trans Antennas Propag* 2005;53(9):2865–71.
- [22] Montisci G, Mazzarella G. Full-wave analysis of a waveguide printed slot. *IEEE Trans. Antennas Propag* Aug. 2004;52(8):2168–71.
- [23] Sánchez-Olivares P, Masa-Campos JL. Novel Four Cross Slot Radiator With Tuning Vias for Circularly Polarized SIW Linear Array. *IEEE Trans Antennas Propag* April 2014;62(4):2271–5.
- [24] Kildal P, Alfonso E, Valero-Nogueira A, Rajo-Iglesias E. Local Metamaterial-Based Waveguides in Gaps Between Parallel Metal Plates. *IEEE Antennas Wirel Propag Lett* 2009;8:84–7.
- [25] Balanis C. *Antenna Theory, Analysis and Design*. 3rd Edition. Wiley; 2005.
- [26] Henry R, Okoniewski M. A Broadside Scanning Substrate Integrated Waveguide Periodic Phase-Reversal Leaky-Wave Antenna. *IEEE Antennas Wirel Propag Lett* 2016;15:602–5.